

# SCIENTIFIC REPORTS



OPEN

## A Matrix Pencil Algorithm Based Multiband Iterative Fusion Imaging Method

Yong Qiang Zou<sup>1</sup>, Xun Zhang Gao<sup>1</sup>, Xiang Li<sup>1</sup> & Yong Xiang Liu<sup>2</sup>

Received: 25 August 2015  
Accepted: 11 December 2015  
Published: 19 January 2016

Multiband signal fusion technique is a practicable and efficient way to improve the range resolution of ISAR image. The classical fusion method estimates the poles of each subband signal by the root-MUSIC method, and some good results were get in several experiments. However, this method is fragile in noise for the proper poles could not easy to get in low signal to noise ratio (SNR). In order to eliminate the influence of noise, this paper propose a matrix pencil algorithm based method to estimate the multiband signal poles. And to deal with mutual incoherent between subband signals, the incoherent parameters (ICP) are predicted through the relation of corresponding poles of each subband. Then, an iterative algorithm which aimed to minimize the 2-norm of signal difference is introduced to reduce signal fusion error. Applications to simulate dada verify that the proposed method get better fusion results at low SNR.

Multiband radar signal fusion (MRSF) technique is an efficient way to get high resolution ISAR image at the state of the art<sup>1-3</sup>. Unlike construct a ultrawide band radar, it expands the echo signal frequency band by filling the gap data at the signal level, which is more flexible and economical. Meanwhile, the MRSF brings some challenges for ISAR imaging algorithms<sup>4-8</sup>. Two important questions are multiband signal coherent compensation<sup>9,10</sup> and damped exponential (DE) model parameter estimation<sup>11</sup>.

For the first question, the subband signals are derived from different wideband radars, and the coherent between them cannot be well guaranteed even though high precision synchronization techniques are adopted<sup>12,13</sup>. However, high accuracy coherent is crucial for radar imaging, and if lack of compensation, the the target radar images would be defocused and blurring, and it would not be imaged in serious cases. This issue arouse great concern among researchers, and several compensation methods were proposed. Cuomo<sup>11</sup> in Lincoln laboratory analysed a wide variety of factors which relate to mutual incoherent, and proved that there were a fixed phase and a linear phase (these two factors are the so-called ICP) between two incoherent subband signals. In ref. 11, a modified root-MUSIC and least square algorithm are used to construct DE model of each subband signal. Depending on these models, each subband is extrapolated to get full band signals, then high dimension optimization is applied to find the fixed phase and the linear phase. However, big error would be introduced by the extrapolation when the gap band is wide. In ref. 14, the similarity between high range resolution profile (HRRP) of the subband is utilized to estimate the linear phase, and then a cost function is defined to derive the fixed phase. This method has high calculate efficiency, but the estimation precision is related to the sample number. In refs 9,10, the fixed phase and linear phase were deduced through the corresponding poles expressions which relate to the same scattering centers. Extrapolation error does not exist here, and the calculation burden is also reduced.

For the second question, the DE model is usually transformed to all-pole model and the parameters are estimated by the modified root-MUSIC and least square algorithm<sup>9,11</sup>. In ref. 9,11, the poles closest to the unit circle are used to characterize the subband signals, but this principle is not suitable at low SNR cases, for some interference poles may be selected. Once some false poles are chosen, it is hard to avoid big error in poles estimation. Apart from that, Piou<sup>15</sup> proposed a state-space based method. In his algorithm, a set of matrices that best describe the measured data are determined, and the fitted data are used to interpolate between and extrapolate outside of the measurement bands. And at the meanwhile, he also presented an iterative approach that refines the

<sup>1</sup>School of Electronics Science and Technology, National University of Defense Technology, Changsha, 410073, China.

<sup>2</sup>Research Institute of Space Electronics Technology, National University of Defense Technology, Changsha, 410073, China. Correspondence and requests for materials should be addressed to Y.Q.Z. (email: zouyongqiangnurd@yeah.net)

state-space matrices of the dual band and improves the fitted data in the vacant bands. But this method faced the same problem at low SNR environment.

In order to solve the aforementioned problems, matrix pencil algorithm which has better performance at low SNR is adopted to estimate the poles and its amplitudes. Then the difference between correspond poles of incoherent signals is analyzed, and a high accuracy coherent compensation approach which does not depend on signal extrapolation and sample numbers is proposed. In order to improve the signal fusion precision, an iterative signal fusion process which aimed to minimize the 2-norm of signal difference is introduced. At last, some simulate experiments are carried out to verify the effective of the method.

## Methods

**Multiband Signals Coherent Compensation.** In ref. 9, Tian proposed a novel method to estimate the ICP, however, the phase variety caused by the vacant band is not taken into considered, meanwhile the poles estimated by the root-MUSIC method is easily affected by the noise, both of them would result in loss of precision. In this section, a modified method is proposed.

Without loss of generality, considering the fusion of two subbands, ICP are added to the higher subband. For a static target with  $M$  scattering centers, the baseband echo signal of the lower and higher subbands  $s_1, s_2$  can be written as

$$s_1(k) = \sum_{m=1}^M A_m \left( \frac{f_k}{f_1} \right)^{\alpha_m} \exp \left( -j \frac{4\pi f_k r_m}{c} \right), k = 0, \dots, N_1 - 1 \quad (1)$$

$$s_2(k') = \sum_{m=1}^M A_m \left( \frac{f_{k'}}{f_2} \right)^{\alpha_m} \exp \left( -j \frac{4\pi f_{k'} r_m}{c} \right) \cdot \exp(j\eta + jk'\theta), k' = 0, \dots, N_2 - 1 \quad (2)$$

where  $f_1, f_2$  are the start frequencies of the two subbands,  $N_1, N_2$  are the step numbers, and the step frequency is  $\Delta f, f_2 = f_1 + \Delta B, \Delta B > \Delta f \cdot N_1$ . Obviously, Eq. (1) and (2) are the geometrical theory of diffraction model (GTD) expression of  $s_1, s_2$ , respectively. The model parameters  $\{A_m, r_m, \alpha_m\}_{m=1}^M$  characterize the scattering centers, and  $A_m$  denotes the scattering center amplitude,  $r_m$  is the relative range of scattering center with respect to the reference point,  $\alpha_m$  is the frequency depend factor (FDF), which denotes the kind of scattering center.  $f_k = f_1 + k \cdot \Delta f, f_{k'} = f_2 + k' \cdot \Delta f, c$  is the velocity of light.  $\eta, \theta$  are the ICP, i.e. the aforementioned fixed phase and linear phase.

Although Eq. (1) and (2) describe the subband signals precisely, it is hard to estimate the parameters accurately due to the FDF. In this paper, the power function  $f^{\alpha_m}$  is replaced by the exponential function  $\beta_m^f$ , then the GTD model is transformed into DE model, and it can be expressed as all-pole model further (see Eqs (3) and (4)).

$$\begin{aligned} s_1(k) &\approx \sum_{m=1}^M A_m \left( \frac{j}{f_1} \right)^{\alpha_m} \beta_m^{f_k} \exp \left( -j \frac{4\pi f_k r_m}{c} \right) \\ &= \sum_{m=1}^M A_m \left( \frac{j}{f_1} \right)^{\alpha_m} \beta_m^{f_1} \exp \left( -j \frac{4\pi f_1 r_m}{c} \right) \cdot \left( \beta_m^{\Delta f} \exp \left( -j \frac{4\pi \Delta f r_m}{c} \right) \right)^k \\ &= \sum_{m=1}^M b_m \cdot p_m^k, k = 0, \dots, N_1 - 1 \end{aligned} \quad (3)$$

$$\begin{aligned} s_2(k') &\approx \sum_{m=1}^M A_m \left( \frac{j}{f_2} \right)^{\alpha_m} \beta_m^{f_{k'}} \exp \left( -j \frac{4\pi f_{k'} r_m}{c} \right) \exp(j\eta + jk'\theta) \\ &= \sum_{m=1}^M A_m \left( \frac{j}{f_2} \right)^{\alpha_m} \beta_m^{f_2} \exp \left( -j \frac{4\pi f_2 r_m}{c} + j\eta \right) \\ &\quad \cdot \left( \beta_m^{\Delta f} \exp \left( -j \frac{4\pi \Delta f r_m}{c} + j\theta \right) \right)^{k'} \\ &= \sum_{m=1}^M d_m \cdot q_m^{k'}, k' = 0, \dots, N_2 - 1 \end{aligned} \quad (4)$$

where  $p_m$  and  $q_m$  denote the poles of  $s_1, s_2, b_m, d_m$  are the corresponding amplitudes.

As a matter of fact, the all-pole model is essentially the summation of harmonic, many harmonic decomposition algorithms can be employed to estimate the parameters, and matrix pencil (MP) is one of the better methods. It was first presented by Y.B.Hua and T.K.Sarkar<sup>16</sup>, and often regarded as one variation of estimating signal parameter via rotational invariance techniques (ESPRIT). It utilizes the properties of exponent signal to estimate the amplitudes and poles simultaneously by solving the generalized eigenvalues of matrix pencil. Through the comparative study of MUSIC, root-MUSIC, ESPRIT, and MP<sup>17–19</sup>, we can draw the conclusion that the MP algorithm

has a better performance than the others at low SNR. Then, in this paper, the poles and its amplitudes are solved by MP method.

Taking  $s_1$  as an example, the Hankel matrix should be constructed first, i.e.

$$X_0 = (D_{M_0-1}, D_{M_0-2}, \dots, D_0), X_1 = (D_{M_0}, D_{M_0-1}, \dots, D_1) \tag{5}$$

where  $D_k = [s_1(k), s_1(k+1), \dots, s_1(N - M_0 + k - 1)]^T$ ,  $M_0$  is the pencil parameter, and  $\hat{M} \leq M_0 \leq N_1 - \hat{M}$ . The model order  $\hat{M}$  can be obtained by minimum description length (MDL) or Akaike information criterion (AIC) methods, and then the singular value decomposition (SVD) of  $X_0$  and  $X_1$  are given by

$$X_0 = [U_0, U'_0] \begin{bmatrix} \Delta_{\hat{M}} & 0 \\ 0 & \Delta_{M_0-\hat{M}} \end{bmatrix} [V_0, V'_0], X_1 = [U_1, U'_1] \begin{bmatrix} \Sigma_{\hat{M}} & 0 \\ 0 & \Sigma_{M_0-\hat{M}} \end{bmatrix} [V_1, V'_1] \tag{6}$$

where  $\Delta_{\hat{M}}, \Sigma_{\hat{M}}$  are the diagonal matrix composed by the first  $\hat{M}$  main singular values of  $X_0, X_1$ , respectively. They and the corresponding matrix  $U_0, V_0, U_1, V_1$  contain the signal information and a little noise information. While  $\Delta_{M_0-\hat{M}}, \Sigma_{M_0-\hat{M}}$  are the diagonal matrix composed by the rest  $M_0 - \hat{M}$  singular values of  $X_0, X_1$ , they and the corresponding matrix  $U'_0, V'_0, U'_1, V'_1$  contain noise information only.

If

$$X_{0s} = U_0 \Delta_{\hat{M}} V_0, X_{1s} = U_1 \Sigma_{\hat{M}} V_1 \tag{7}$$

Then the poles  $\{\hat{p}_m\}_{m=1}^{\hat{M}}$  can be estimated by solving the generalized eigenvalues of  $X_{1s} - \lambda X_{0s}$ , and the amplitude  $\{\hat{b}_m\}_{m=1}^{\hat{M}}$  are given by:

$$[\hat{b}_1, \dots, \hat{b}_{\hat{M}}]^T = (\tilde{P}^H \tilde{P})^{-1} \tilde{P}^H [s(0), \dots, s(N_i - 1)]^T \tag{8}$$

where  $\tilde{P} = \begin{bmatrix} \hat{p}_1^0 & \dots & \hat{p}_{\hat{M}}^0 \\ \vdots & \ddots & \vdots \\ \hat{p}_1^{N_i-1} & \dots & \hat{p}_{\hat{M}}^{N_i-1} \end{bmatrix}$  is a Vandermonde matrix composed by the  $\hat{M}$  poles.

The poles of  $s_1, s_2$  are given below:

$$\hat{p}_m = \beta_m^{\Delta f} \exp\left(-j \frac{4\pi \Delta f r_m}{c}\right), \hat{q}_m = \beta_m^{\Delta f} \exp\left(-j \frac{4\pi \Delta f r_m}{c} + j\theta\right) \tag{9}$$

From Eq. (9), it is clearly that the only difference between the same order poles of  $s_1$  and  $s_2$  is a linear phase  $\theta$ , and it is given by:

$$\hat{\theta} = \frac{\sum_{m=1}^{\hat{M}_{\min}} \arg(\hat{q}_m) - \sum_{m=1}^{\hat{M}_{\min}} \arg(\hat{p}_m)}{\hat{M}_{\min}} \tag{10}$$

where  $\hat{M}_{\min} = \min(\hat{M}_1, \hat{M}_2)$ ,  $\hat{M}_1, \hat{M}_2$  are the estimated poles numbers of each subband, respectively. And  $\arg(\cdot)$  denotes the phase of complex.

Similarly, the amplitudes  $\hat{b}_m, \hat{d}_m$  are given by:

$$\hat{b}_m = A_m \left(\frac{j}{f_1}\right)^{\alpha_m} \beta_m^{f_1} \exp\left(-j \frac{4\pi f_1 r_m}{c}\right), \hat{d}_m = A_m \left(\frac{j}{f_2}\right)^{\alpha_m} \beta_m^{f_2} \exp\left(-j \frac{4\pi f_2 r_m}{c} + j\eta\right) \tag{11}$$

Obviously, the amplitudes are more complex than the poles. Their phases are determined by the fixed phase, the start frequency  $(f_1, f_2)$ , FDF  $\alpha_m$  and relative ranges  $r_m$ , i.e.

$$\arg(\hat{b}_m) = \arg\left(\left(\frac{j}{f_1}\right)^{\alpha_m}\right) - \frac{4\pi f_1 r_m}{c}, \arg(\hat{d}_m) = \arg\left(\left(\frac{j}{f_2}\right)^{\alpha_m}\right) - \frac{4\pi f_2 r_m}{c} + \eta \tag{12}$$

The exact numeric values of  $\arg\left(\left(\frac{j}{f_l}\right)^{\alpha_m}\right)$  ( $l = 1, 2$ ) cannot be given, for  $\alpha_m$  is unknown. Nevertheless, the following relation is satisfied.

$$\arg\left(\left(\frac{j}{f_l}\right)^{\alpha_m}\right) = \arg\left(\left(\frac{1}{f_l}\right)^{\alpha_m} j^{\alpha_m}\right) = \arg(j^{\alpha_m}), l = 1, 2 \tag{13}$$

And  $f_2 = f_1 + \Delta B$ , then the fixed phase is given by Eq. (14), i.e.,

$$\hat{\eta} = \frac{\sum_{m=1}^{\hat{M}_{\min}} \arg(\hat{d}_m) - \sum_{m=1}^{\hat{M}_{\min}} \arg(\hat{b}_m) + \frac{4\pi \Delta B}{c} \sum_{m=1}^{\hat{M}_{\min}} \hat{r}_m}{\hat{M}_{\min}} \tag{14}$$

where  $\sum_{m=1}^{\hat{M}} \hat{r}_m = \frac{C}{4\pi\Delta f} \sum_{m=1}^{\hat{M}} \arg(\hat{p}_m)$

When substituting  $\hat{\eta}, \hat{\theta}$  into Eq. (15), the higher subband signal is compensated.

$$\hat{s}_2 = s_2 \cdot \exp(-j\hat{\eta} - jk'\hat{\theta}), k' = 0, \dots, N_2 - 1 \tag{15}$$

The parameter precision are guaranteed by two aspects:

1. Due to the MP algorithm has good anti-noise performance, the estimate results is interfered slightly and more robust.
2. There is no data extrapolation in this approach, which reduce estimation error.

**Multiband Radar Signal Fusion Imaging.** In ref. 9, the band gap is filled by GAPES<sup>20</sup>, and a full band all-pole model is constructed by the modified root-MUSIC, then the fusion images of simulate data are obtained. However, there is no feedback in this algorithm, which is more important for improving the parameter estimation precision. In this section, the full band all-pole model is obtained by MP, and then the gap data is filled by the all-pole model. After that, the initial fusion results are feedback to the previous step until the fusion precision fulfills the requirement.

If  $s_1, s_2$  are two subband signals whose length are  $N_1, N_2$ , respectively.  $\Delta B$  is the band gap between them, and  $N$  is the samples number of the full band signal. Our fusion approach contains the following steps:

- (1) Compensate  $s_2$  with the aforementioned coherent compensation approach, then we get  $\hat{s}_2$  which is coherent with  $s_1$ . For the sake of simplicity, let  $s_2 = \hat{s}_2$ , i.e.,  $s_2$  denotes  $\hat{s}_2$  in the following steps.
- (2) Construct the full band all-pole model by  $s_1, s_2$ . The full band all-pole model is

$$s(k) = \sum_{m=1}^M b_m \cdot p_m^k, k = 0, \dots, N - 1 \tag{16}$$

The parameters of Eq. (16) are also estimated by MP, but there are two signals and their frequency band are not overlapped. So the Hankel matrices are constructed a bit differently. Let

$$\begin{cases} X_{i0} = (D_{M_0-1}^i, D_{M_0-2}^i, \dots, D_0^i) \\ X_{i1} = (D_{M_0}^i, D_{M_0-1}^i, \dots, D_1^i) \end{cases} \tag{17}$$

where  $D_k^i = [s_i(k), s_i(k + 1), \dots, s_i(N - M_0 + k - 1)]^T, i = 1, 2$ .  
And the Hankel matrices are

$$X_0 = \begin{bmatrix} X_{10} \\ X_{20} \end{bmatrix}, X_1 = \begin{bmatrix} X_{11} \\ X_{21} \end{bmatrix} \tag{18}$$

The following parameters estimation process can refer to the previous section.

- (3) After the poles and the amplitudes are obtained, the full band signal can be estimated by Eq. (19):

$$\hat{s}(k) = \sum_{m=1}^{\hat{M}} \hat{b}_m \cdot \hat{p}_m^k, k = 0, \dots, N - 1 \tag{19}$$

Then the initial estimated subband signals are

$$\begin{cases} \hat{s}_1(k) = \hat{s}(k), k \in [0, N_1 - 1] \\ \hat{s}_g(k) = \hat{s}(k), k \in [N_1, N - N_2 - 1] \\ \hat{s}_2(k) = \hat{s}(k), k \in [N - N_2, N - 1] \end{cases} \tag{20}$$

In order to reduce the estimate error, substitute  $\hat{s}_1, \hat{s}_2$  with  $s_1, s_2$ , and the initial full band fusion signal is written below:

$$\begin{cases} s_1(k), k \in [0, N_1 - 1] \\ \hat{s}_g(k), k \in [N_1, N - N_2 - 1] \\ s_2(k), k \in [N - N_2, N - 1] \end{cases} \tag{21}$$

- (4) Iterate the fusion result. During each iteration, the approach evaluates the error energy between the estimated signal and primary simulate signal, and the error energy is defined by

$$E_i = \|\hat{s}_1^i - s_1\|_2 + \|\hat{s}_2^i - s_2\|_2 \tag{22}$$

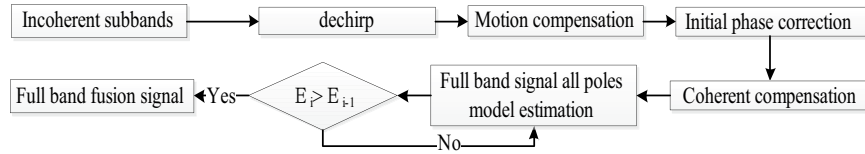


**Figure 1. Multiband iterative fusion flow chart.**

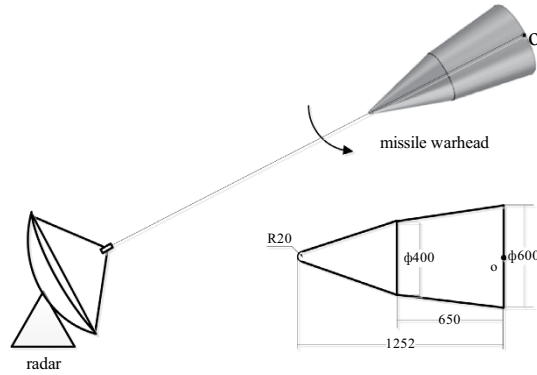


**Figure 2. Missile warhead model.**

where  $\hat{s}_1^i$  and  $\hat{s}_2^i$  denote the estimated values of the primary simulate signal  $s_1$  and  $s_2$ , respectively. If  $E_i \leq E_{i-1}$ , then the algorithm generates a new full band fusion signal based on the  $i - th$  iteration fusion signal. If  $E_i > E_{i-1}$ , the algorithm stops, and the  $(i - 1) - th$  iteration full band fusion signal is just the final result.

The flow chart of the proposed algorithm is illustrated Fig. 1, and before coherent compensation several pre-process are added. While this section discuss the processing for only two subbands, it is straightforward to apply this concept to an arbitrary number of subbands.

The full band fusion HRRP can be obtained by apply the pulse compression to the final fusion signal. After that, if we apply pulse compression in cross-range, then the fusion ISAR image is obtained.

## Results

**Model and Simulate Parameter.** In order to test the algorithm, the proposed method (A1 for short), the approach in ref. 11 (A2 for short), the approach in ref. 9 (A3 for short), and the approach in ref. 15 (A4 for short) are applied to the GTD model based simulate data and the missile warhead electromagnetic computation model data to fuse multiband signals and obtain the radar ISAR images.

Coherent compensation and HRRP fusion test are carried out on the GTD model based simulated data. And the start frequency  $f_0 = 8GHz$ , step frequency  $\Delta f = 10MHz$ , step number  $N = 300$ , the bandwidth  $B = 3GHz$  (the theory range resolution is 0.05 m). The target is composed of three scattering centers, the scattering intensity are 2, 1.5, 2.5, respectively. And the FDF and the relative ranges relate to the reference range are  $-1, 1, -0.5$  and 0.97, 1.05, 1.24, respectively. Then the baseband noisy signal is

$$s(k) = \sum_{m=1}^3 A_m \left( \frac{f_k}{f_0} \right)^{\alpha_m} \exp \left( -j \frac{4\pi f_k r_m}{c} \right) + e(k), k \in [0, N), k \in N^+ \tag{23}$$

where  $f_k = f_0 + k\Delta f$ ,  $e(k)$  is zero mean white Gauss noise.

After that, a missile warhead model is constructed in CST2012 environment, and the sweep frequency data of different aspect angle is obtained. This model is a simple missile warhead (Fig. 2). Here the aspect angle is  $0^\circ \sim 180^\circ$  when the warhead rotate counter-clockwise. The parameters are set as follows: aspect angles are  $0^\circ \sim 10^\circ$  with angle interval  $0.1^\circ$ , frequency range from  $10GHz$  to  $14GHz$  with frequency interval  $20MHz$ . Matrix  $X$  denotes the electromagnetic computation data, then the number of its column and row are 201 and 101, respectively.

**Multiband Signals Coherent Compensation Experiment.** Letting

$$\begin{cases} s_1(k) = s(k), k \in [0, N/3) \\ s_m(k) = s(k), k \in [N/3, 2N/3) \\ s_2(k) = s(k), k \in [2N/3, N) \end{cases} \tag{24}$$

In order to simulate the effect of mutual incoherence, the higher subband signal  $s_2(k)$  is modulated by  $\exp(j\eta + jk\theta)$ , i.e.,

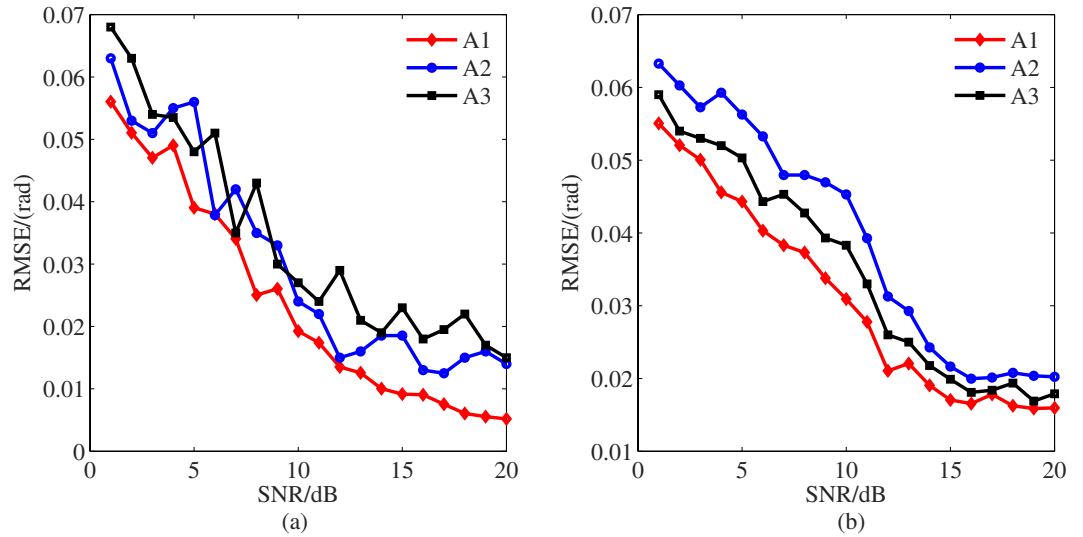


**Figure 3. Incoherent parameter estimation result. (a) fixed phase estimation result. (b) linear phase estimation result.**

$$s_2'(k) = s_2(k) \exp(j\eta + jk\theta) \tag{25}$$

where  $\eta = \pi/8, \theta = \pi/9$ . The aforementioned algorithms are applied to estimate  $\eta$  and  $\theta$  at  $SNR = 1 \sim 20dB$  (As approach A4 does not give its coherent compensation method, so this part of test are only carried out on the other three algorithms). Figure 3 illustrates the results of 100 runs Monte Carlo simulation. From Fig. 3, it is obviously that the RMSE of  $\hat{\eta}$  and  $\hat{\theta}$  are increased as the SNR decrease, and in general, A1 has the lowest RMSE. It is obviously that the proposed method improves the parameter precision at low SNR, which verifies the analysis in previous section.

After coherent compensation,  $s_1, s_2$  are mutual coherent, the four algorithms are applied to get the gap data at  $SNR = 15dB$ . Figure 4 illustrates the estimated gap data  $s_m$  and the primary simulate data. From this figure, all the algorithms can fit the primary data to a certain extent. In general, the result of A1 is better than the other three, and the suboptimal estimated signal is the result of A4. A1 and A4 share one thing in common: they all contain iteration process, and the results show that this process can significantly decrease the fitting error. At the meanwhile, the results also proof the MP method is more efficient than the state-space method in noisy environment.

Denote  $s_m$  as the estimated data, and the final full band signal  $\tilde{s}$  can be derived by  $s_1, s_m, s_2$  according to Eq. (24). Figure 5 illustrates the real wave and HRRP of  $s$  and  $\tilde{s}$ . It is hard to recognize the first and the second scattering point in subband HRRPs due to the bandwidth of each subband is 1 GHz, and after the gap data is filled, the full band fusion HRRP can do it easily, which verifies the proposed method improve the range resolution.

**Multiband ISAR Imaging Experiment.** Letting

$$X_1 = \begin{bmatrix} x_{1,1} & x_{1,2} & \cdots & x_{1,101} \\ x_{2,1} & x_{2,2} & \cdots & x_{2,101} \\ \vdots & \vdots & & \vdots \\ x_{51,1} & x_{51,2} & \cdots & x_{51,101} \end{bmatrix}, X_2 = \begin{bmatrix} x_{151,1} & x_{151,2} & \cdots & x_{151,101} \\ x_{152,1} & x_{152,2} & \cdots & x_{152,101} \\ \vdots & \vdots & & \vdots \\ x_{201,1} & x_{201,2} & \cdots & x_{201,101} \end{bmatrix} \tag{26}$$

The frequency band range of  $X_1$  and  $X_2$  are 10GHz ~ 11GHz and 13GHz ~ 14GHz, respectively. Figure 6 illustrates the subband ISAR images and the full band ISAR images at two different SNR. It is hard to get the precision position of each scattering center due to the poor range resolution of Fig. 6(a,b).

Similarly,  $X_2$  is modulated with the ICP, and  $\eta = \pi/8, \theta = \pi/9$ . Apply the four algorithms to  $X_1$  and  $X_2$  at  $SNR = 15dB$  and  $SNR = 10dB$ , and the fusion results are illustrated in Figs 7 and 8.

Obviously, compared with Fig. 6, the range resolution of the fusion ISAR images in Fig. 7 is improved significantly, and most scattering centers can be positioned precisely. However, in this figure, the fusion images are defocused at different level which result that some scattering points become blurred, such as the second point in the middle of Fig. 7(c). And for Fig. 7(b), there are strong shadows around some points. Owe to the iteration process, Fig. 7(a,d) have the better focused effect, but the shadow of Fig. 7(d) is a little more than Fig. 7(a). Comparatively speaking, Fig. 7(a) is more similar to the original ISAR image (Fig. 6(c)) than the other three.

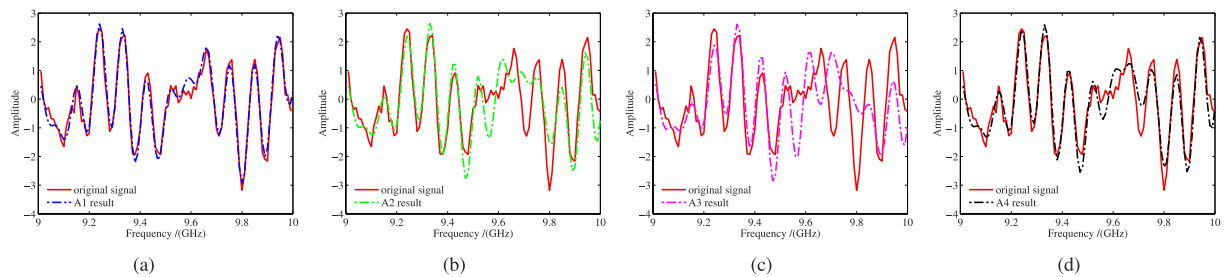


**Figure 4. The gap band estimate result.** (a) the result of A1. (b) the result of A2. (c) the result of A3. (d) the result of A4.

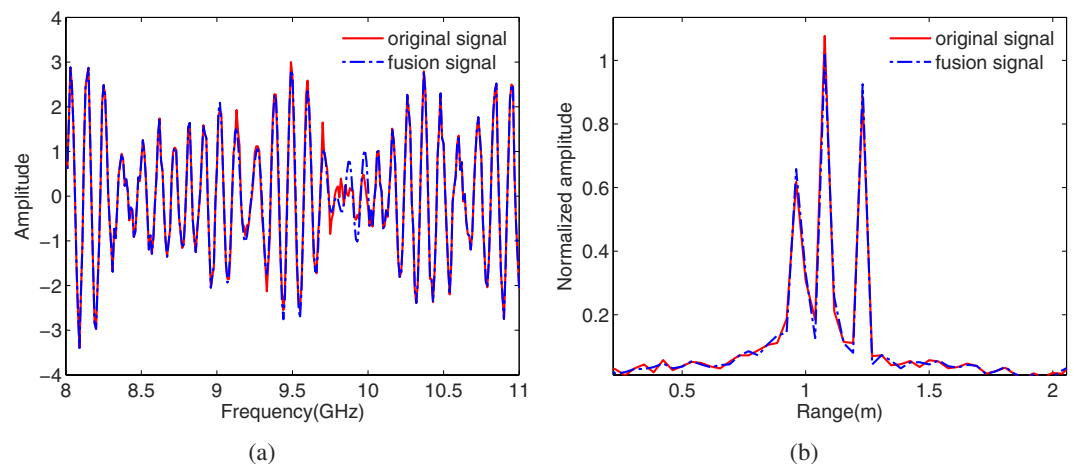


**Figure 5. The final full band fusion result of the proposed method.** (a) real wave. (b) HRRP

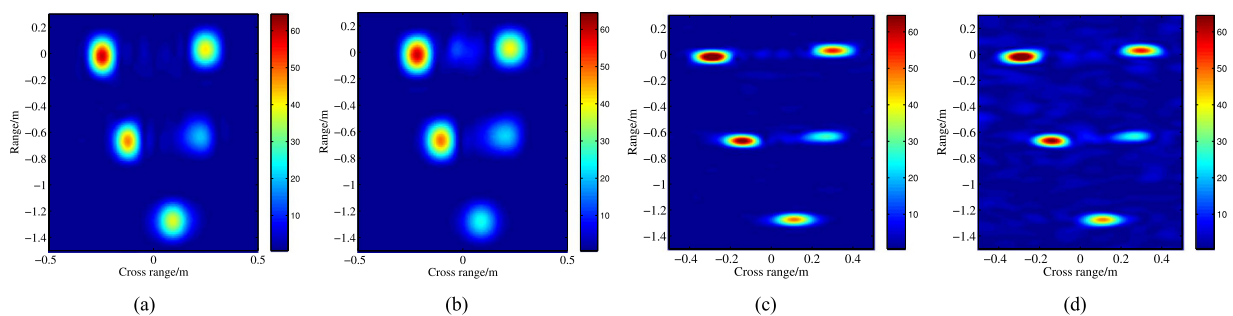


**Figure 6. Missile warhead ISAR images.** (a) lower band ( $X_1$ ); (b) higher band ( $X_2$ ); (c) full band (SNR = 15 dB); (d) full band (SNR = 10 dB).

As the SNR decrease to 10dB, the original noisy ISAR image (Fig. 6(d)) is still clear, but the quality of the fusion image is degraded seriously. Although the range resolution of the fusion images in Fig. 8 is improved, a lot of strong false scattering centers emerge. For Fig. 8(b,c), it is hard to distinguish some false scattering centers from the true points. And Fig. 8(a,d) has the similar result, but the latter has more false points. Then it is obviously that Fig. 8(a) is more better than Fig. 8(b-d).

Table 1 list the image entropy<sup>21</sup> of each ISAR images in Figs 7 and 8. The ISAR image entropy indicates the quality of the image, and the image which has the smaller entropy is better than the larger one. Then from Table 1, we can conclude that the results are consistent with the former analysis.

Above mentioned results show that the MP method and the iteration process have better fusion precision than the other three algorithms at the same SNR.

**Band Gap and The Fusion ISAR Images.** In this section, the bound of multiband fusion with different subband width and gap width is discussed through the simulated experiments. The missile warhead model electromagnetic computation data is adopted, and all the four algorithms are applied to the subband data which has different gap to total band ratio (i.e.,  $GTBR$ , and it defined as  $GTBR = \frac{gap}{totalband} \times 100\%$ ) at SNR = 20dB. Here,

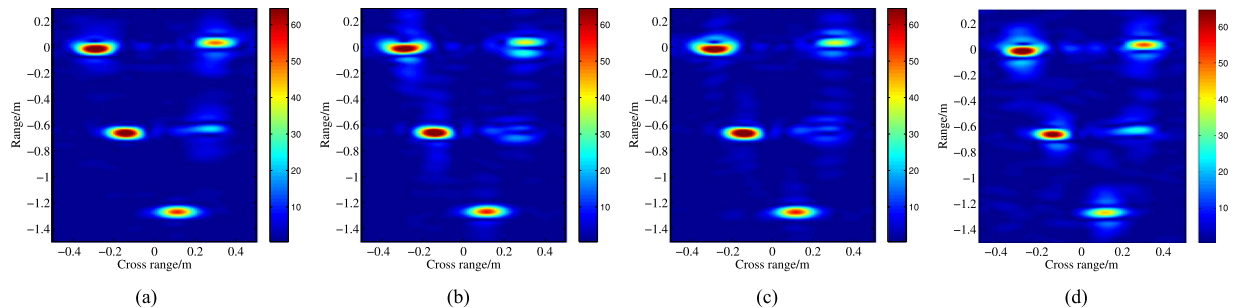


**Figure 7.** ISAR image of the missile model (SNR = 15 dB). (a) the fusion full band ISAR image (A1); (b) the fusion full band ISAR image (A2); (c) the fusion full band ISAR image (A3); (d) the fusion full band ISAR image (A4).

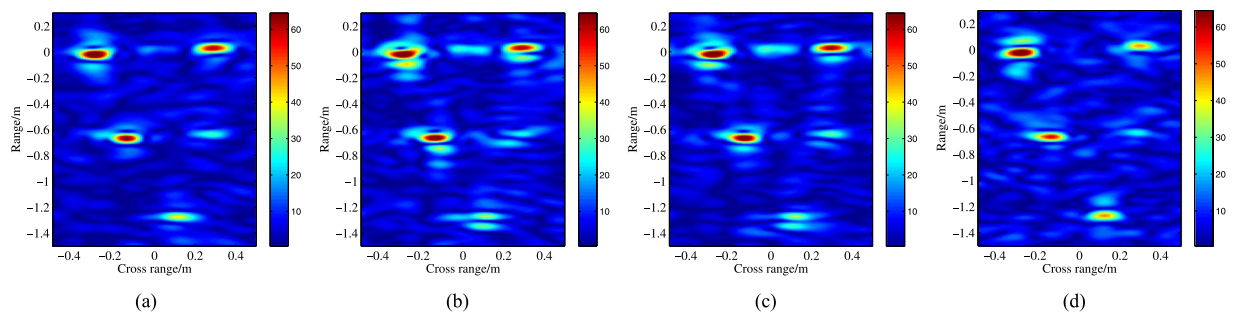


**Figure 8.** ISAR image of the missile model (SNR = 10 dB). (a) the original ISAR image. (b) the fusion full band ISAR image (A1); (c) the fusion full band ISAR image (A2); (d) the fusion full band ISAR image (A3).

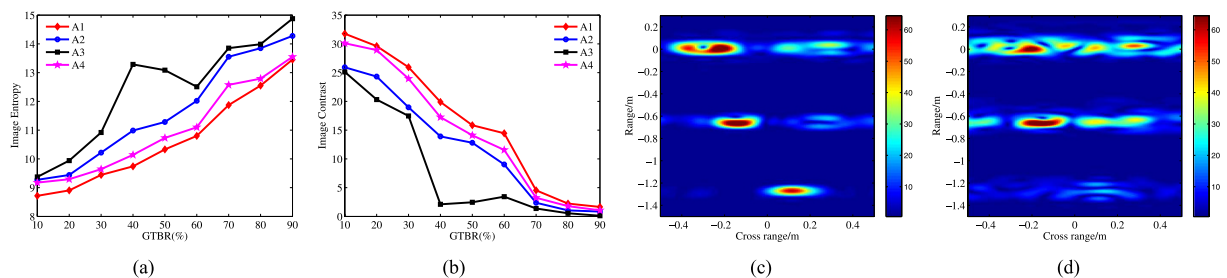


**Figure 9.** The infection of band gap to ISAR fusion images (SNR = 20 dB). (a) the image entropy with different GTBR. (b) the image contrast with different GTBR; (c) the fusion ISAR image of A1 at GTBR = 60%; (d) the fusion ISAR image of A1 at GTBR = 70%.

SNR (dB)	noisy primary signal	A1 results	A2 results	A3 results	A4 results
15	10.3679	11.1461	11.9137	11.8158	11.2824
10	11.2536	12.3927	12.9788	12.7942	12.5729

**Table 1.** ISAR Image Entropy.

image entropy and image contrast<sup>21</sup> are used to indicate the quality of the fusion ISAR images, and commonly speaking, the image entropy should be as small as possible, while for the image contrast, the larger the better. The results after 100 Monte Carlo simulations are illustrated in Fig. 9. In Fig. 9(a,b), the image entropy increases as the GTBR grows, and the image contrast decreases as the GTBR grows, which tell that wide gap bring great difficulties to fusion imaging algorithms. From these two figures, an obvious transformation takes place at GTBR = 60 ~ 70% (the results of A3 fluctuate fiercely, but in this range it also has a great change). The fusion ISAR images of A1 at these two GTBR are illustrated in Fig. 9(c,d). Figure 9(d) has serious defocused, and the intensities of some false scattering points even stronger than the true points, so it is hard to recognize the target from it. Relatively



speaking, although Fig. 9(c) is defocused, most of the true scattering points can be recognized. If we choose  $GTBR = 60\%$  as the critical value for A1, then the other algorithms' critical values which have the similar image entropy and image contrast are  $GTBR = 50\%(A2)$ ,  $GTBR = 30\%(A3)$  and  $GTBR = 60\%(A4)$ , respectively.

## Discussion

In this paper, MP method is used to estimate the all-pole model parameters which ensure the parameter accuracy at low SNR conditions. After that, two equations are deduced to calculate the incoherent parameters, which can elevate the precision of coherent compensation. What is more, a 2-norm based iterative process is introduced to improve the signal fusion precision. The simulate tests indicate that compared with the other fusion methods, the proposed method can give better fusion signal in low SNR environment. Apart from that, the bound of multiband fusion with different subband width and gap width is also analysed, and the critical values of different algorithms are given in the aforementioned environment. However, although our method has better antinoise capability, it can not work well in colored noise environment, so a modified version of our method should be studied to tackle this problem. At the meanwhile, the present method need a large amount of calculation which impose heavy burden on computers, and it is not suitable for real time process, so in the next step, how to decrease the calculation should be discussed.

## References

1. Naishadham, K. & Piou, J. State-space spectral estimation of characteristic electromagnetic responses in wideband data. *IEEE Antennas Wireless Propagat. Lett.* **4**, 406–409 (2005).
2. Sacchi, M., Ulrych, T. & Walker, C. Interpolation and extrapolation using a high-resolution discrete fourier transform. *IEEE Trans. Signal Processing* **46**, 31–38 (1998).
3. Wang, Q., Wu, R., Xing, M. & Bao, Z. A new algorithm for sparse aperture interpolation. *IEEE Geosci. Remote. S.* **4**, 480–484 (2007).
4. He, F. & Xu, X. High-resolution imaging based on coherent processing for distributed multi-band radar data. *PIER* **141**, 383–401 (2013).
5. van Dorp, P., Ebeling, R. & Huizing, A. High resolution radar imaging using coherent multiband processing techniques. In *Radar Conference, 2010 IEEE*. Washington DC, United states. Piscataway:Institute of Electrical and Electronics Engineers Inc. 981–986 (2010).
6. Xu, X. & Li, J. Ultrawide-band radar imagery from multiple incoherent frequency subband measurements. *Syst. Eng. Electron.* **22**, 398–404 (2011).
7. Tian, J., Sun, J., Wang, G., Wang, Y. & Tan, W. Multiband radar signal coherent fusion processing with iaa and apfft. *IEEE Signal Processing Lett.* **20**, 463–466 (2013).
8. Bai, X., Zhou, F., Wang, Q., Xing, M. & Bao, Z. Sparse subband imaging of space targets in high-speed motion. *IEEE Trans. Geosci. Remote Sens.* **51**, 4144–4154 (2013).
9. Tian, B., Chen, Z. & Xu, S. Sparse subband fusion imaging based on parameter estimation of geometrical theory of diffraction model. *IET Radar Sonar Navig.* **8**, 318–326 (2014).
10. Tian, B., Liu, Y., Xu, S. & Zengping, C. Multi-band fusion imaging based on high precision parameter estimation of geometrical theory of diffraction model. *Electron. Inf. Tech.* **35**, 1532–1539 (2013).
11. Cuomo, K. M., Piou, J. E. & Mayhan, J. T. Ultra-wideband coherent processing. *IEEE Trans. Antennas Propagat.* **47**, 1095–1107 (1999).
12. Sun, P., Tang, J., He, Q. & Tang, B. Cramer-rao bound of parameters estimation and coherence. *IET Radar Sonar Navig.* **7**, 553–567 (2013).
13. Yang, Y. & Blum, R. S. Phase synchronization for coherent mimo radar: Algorithms and their analysis. *IEEE Trans. Signal Processing* **59**, 5538–5557 (2011).
14. Fu, Y. *et al.* One-dimensional super resolution multi-band radar fusion imaging technology research. *PROG NAT SCI* **16**, 1310–1316 (2006).
15. Piou, J. E., Cuomo, K. M. & Mayhan, J. T. A state-space technique for ultrawide-bandwidth coherent processing. Technical Report 1054, Lincoln Laboratory, Massachusetts Institute Of Technology, Lexington, Massachusetts (1999).
16. Hua, Y. & Sarkar, T. K. Matrix pencil method for estimating parameters of exponentially damped/undamped sinusoids in noise. *IEEE Trans. Acoust. Speech Signal Process.* **38**, 814–824 (1990).
17. Gao, X. *High-Resolution Imaging Method Based on High Order Statistics*. Ph.D. thesis, National University of Defense Technology, Changsha, China (2004).
18. Sarkar, T. K. & Pereira, O. Using the matrix pencil method to estimate the parameters of a sum of complex exponentials. *IEEE Antennas Propagat. Mag.* **37**, 48–55 (1995).
19. Roy, R., Paulraj, A. & Kailath, T. Comparative performance of esprit and music for direction-of-arrival estimation. In *Acoustics, Speech, and Signal Processing, IEEE International Conference on ICASSP '87*. Dallas, USA. New York:IEEE. vol. 12, 2344–2347 (1987).
20. Larsson, E., Liu, G., Stoica, P. & Li, J. High-resolution sar imaging with angular diversity. *IEEE Trans. Aerosp. Electron. Syst.* **37**, 1359–1372 (2001).
21. Martorella, M., Berizzi, F., Palmer, J., Haywood, B. & Bates, B. Image contrast and entropy based autofocusing for polarimetric isar. In *Waveform Diversity and Design Conference, 2007. International*. Pisa, Italy, Piscataway: Institute of Electrical and Electronics Engineers Computer Society. 245–249 (2007).

## Acknowledgements

This work was supported by the National Science Foundation for Distinguished Young Scholars of China (No. 61025006) and the National Natural Science Foundation of China (No. 61422114).

## Author Contributions

Y.Q.Z. provided the idea for this work. Y.Q.Z. and X.Z.G. designed the experiments. Y.Q.Z. performed the experiments and provided all of the figures and data for the paper. Y.X.L. and X.L. prepared the literature and analyzed the results. Y.Q.Z. and X.L. wrote the paper. All authors reviewed the manuscript.

## Additional Information

**Competing financial interests:** The authors declare no competing financial interests.

**How to cite this article:** Zou, Y. Q. *et al.* A Matrix Pencil Algorithm Based Multiband Iterative Fusion Imaging Method. *Sci. Rep.* **6**, 19440; doi: 10.1038/srep19440 (2016).



This work is licensed under a Creative Commons Attribution 4.0 International License. The images or other third party material in this article are included in the article's Creative Commons license, unless indicated otherwise in the credit line; if the material is not included under the Creative Commons license, users will need to obtain permission from the license holder to reproduce the material. To view a copy of this license, visit <http://creativecommons.org/licenses/by/4.0/>